Rapid Fault Leakage Modeling for CO_2 Storage in Saline Aquifers

Hariharan Ramachandran [1*], Iain de Jonge-Anderson [1], Ikhwanul Hafizi Musa [2], Uisdean Nicholson [1], Chee Phuat Tan [3], Sebastian Geiger [4], Florian Doster [1]

[1] Institute of GeoEnergy Engineering, Heriot-Watt University, Edinburgh, UK

[2] PETRONAS Research Sdn Bhd, Bangi, Malaysia

[3] PETRONAS Group Technology & Commercialisation, Kuala Lumpur, Malaysia

[4] Department of Geoscience and Engineering, Delft University of Technology, Delft, Netherlands

* Correspondence: Hariharan Ramachandran, email: h.ramachandran@hw.ac.uk,

X: @hariharram

ORCiD: 0000-0001-5979-0930 (HR)

Rapid Fault Leakage Modeling for CO_2 Storage in Saline Aquifers

Hariharan Ramachandran [1*], Iain de Jonge-Anderson [1], Ikhwanul Hafizi Musa [2], Uisdean Nicholson [1], Chee Phuat Tan [3], Sebastian Geiger [4], Florian Doster [1]

[1] Institute of GeoEnergy Engineering, Heriot-Watt University, Edinburgh, UK

[2] PETRONAS Research Sdn Bhd, Bangi, Malaysia

[3] PETRONAS Group Technology & Commercialisation, Kuala Lumpur, Malaysia

[4] Department of Geoscience and Engineering, Delft University of Technology, Delft, Netherlands

* Correspondence: Hariharan Ramachandran, h.ramachandran@hw.ac.uk

ORCiD: 0000-0001-5979-0930 (HR)

Abstract

Simulating the fluid flow along fault zones at different scales is essential for predicting the CO_2 leakage and containment during injection and storage. However, this can be challenging, especially in the early stages of a storage project when knowledge of the reservoir and caprock is limited and the cost of obtaining the relevant data is high. This study proposes a tool for fast screening of fault leakage at the site screening stage. The tool uses a vertically integrated reservoir model coupled with an upscaled fault leakage function based on source/sink relations. The fault is conceptualized as an increased vertical permeability through the caprock due to the presence of a fracture network in the damage zone and a reduced horizontal permeability in the reservoir due to fault throw and presence of a low-permeability fault core. Simulation results of various CO_2 injection scenarios in a reservoir with potential for fault leakage demonstrate that the tool can produce physically consistent leakage predictions. The computationally efficient model presented in this study is a valuable tool for quantifying uncertainties in key fault parameters, and other constitutive relations that affect the behavior of the storage reservoir and potential fault leakage. By incorporating this tool into the site screening stage, stakeholders

can quickly screen the risk of CO_2 leakage along faults across a range of possible storage sites and subsequently design targeted data acquisition campaigns to better characterize and model the faults. Overall, the proposed tool is a cost-effective and efficient method for screening fault leakage risk during CO_2 injection and storage, helping to ensure safe and effective carbon storage.

Keywords: CO_2 Leakage; Faults; CCS; Vertical Equilibrium Modelling; MRST.

1 Introduction

Storing carbon dioxide (CO_2) in geological formations is a crucial method for mitigating climate change and will be an essential component of a Net Zero Carbon Emission energy landscape in the coming decades (Hepple & Benson, 2004; Krevor et al., 2023). Among the most attractive storage options are saline aquifers, which are widely distributed and possess substantial total storage capacities exceeding gigatons of CO_2 globally (Kumar et al., 2004; Herzog, 2011; Celia et al., 2015). However, successful implementation hinges on the long-term secure containment of CO_2 within these aquifers. Leakage undermines mitigation efforts, poses environmental/health risks, and can erode public trust in Carbon Capture and Storage (CCS) (Bielicki et al., 2014; Ashworth et al., 2015; Jones et al., 2015). Regulatory bodies emphasize the importance of comprehensive geological characterization and storage site assessment to identify significant leakage risk (Dixon et al., 2015; Anderson, 2017; Climate Change Committee, 2021; Romanak & Dixon, 2022). In this context, faults play a crucial role as they can either increase or reduce trapping potential trapping storage, depending on host and fault rock properties. In some cases, by juxtaposing impermeable rock layers, they can function as structural traps, confining the injected CO_2 (Knipe et al., 1998). Conversely, faults also possess the potential to act as leakage pathways that connect the storage reservoir through the overlying caprock to shallower geological layers (Bachu, 2008; Rutqvist, 2012; Snippe et al., 2021). While several successful CCS operations have not encountered significant challenges posed by

faults, the In Salah CCS project exemplifies this risk. CO_2 injection in this project induced seismic activity along a fault, demonstrating the potential for faults to act as pathways for CO_2 leakage (Morris et al., 2011; Ringrose et al., 2013; White et al., 2014; Krevor et al., 2023). As the scale of CCS deployment increases, we will inevitably encounter storage formations containing faults, many of which may be sub-seismic. To expedite the storage site screening, rapid assessment tools are needed to screen for fault-related leakage risks during the early stages of project development.

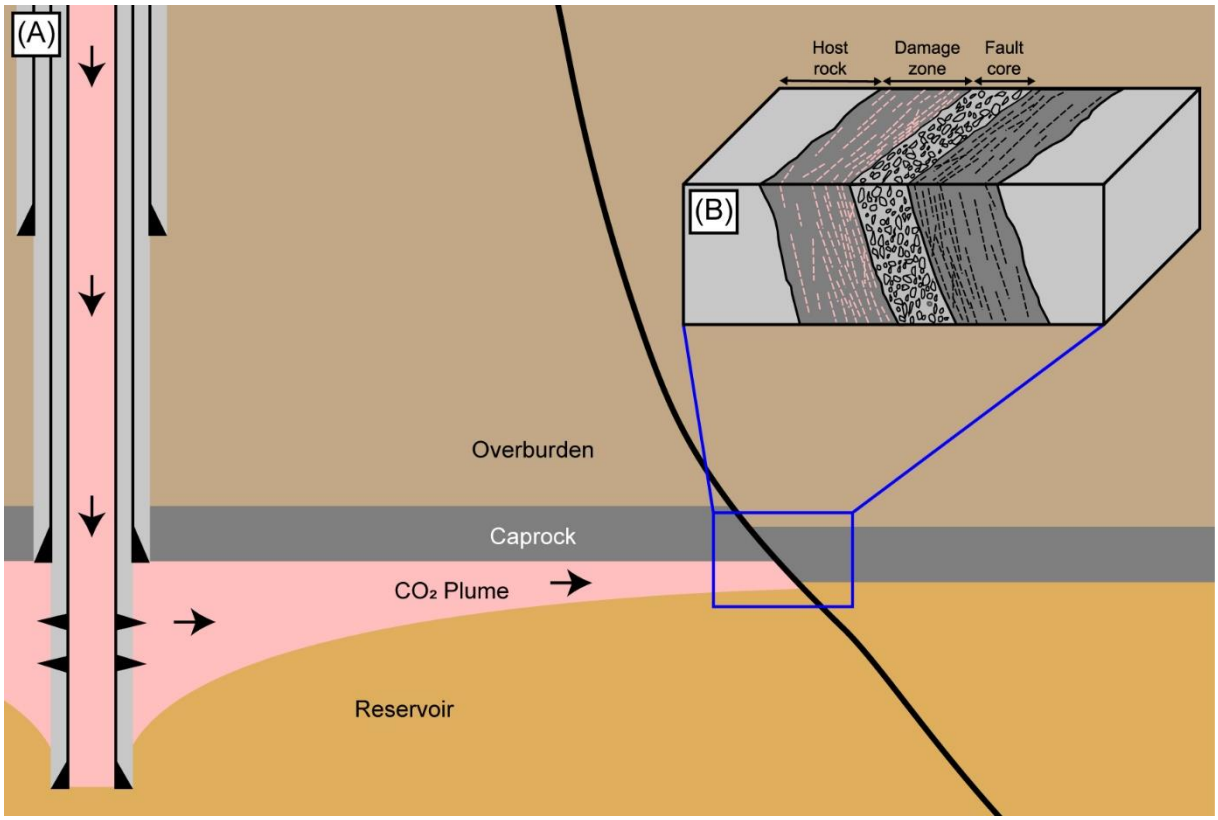

Figure 1 – An illustrative representation of CO_2 storage in a faulted reservoir-caprock system. CO_2 is injected into permeable rock layers spanning hundreds of meters in thickness, with a low-permeability regional seal acting as the primary caprock. The presence of faults can either result in enhanced entrapment, or vertical leakage, depending on fault properties (a). Schematic illustration of fault zone properties, including the fault core and adjacent damage zone (b). Figure adapted from Gasda et al. (2022).

Faults are complex zones of deformation characterized by a central zone of intensely sheared rock, referred to as the fault core, surrounded by a fractured damage zone with a

progressively decreasing fracture density with increasing distance from the fault core (Figure 1) (Sibson, 1977; Gillespie et al., 1993; Walsh et al., 1998; Childs et al., 2009; Faulkner et al., 2010; Phillips et al., 2020). The fault core typically exhibits relatively low permeability because of cataclasis or clay smear (Tueckmantel et al., 2012; Ballas et al., 2015; Dewhurst et al., 2018), while the associated damage zones, dominated by fractures, can exhibit permeabilities several orders of magnitude greater, which can increase their leakage potential (Caine et al., 1996; Childs et al., 2009; Seebeck et al., 2014). The critical factors controlling leakage through faulted zones include fault geometry, architecture, stress regime, rock properties, and fracture density, among others (Rutqvist et al., 2012). Additionally, fault reactivation due to injection-induced changes in pore pressure and stress conditions can potentially generate new leakage pathways/fractures or alter existing ones (Tewari et al., 2023). The sub-seismic nature of these fractures within the damage zone introduces significant uncertainties in CCS operations, as their presence, properties, and ability to form interconnected networks at larger scales remain poorly understood (Rizzo et al., 2024). Furthermore, sub-seismic faults can impede fluid flow and cause unwanted pressure increases within the reservoir or aquifer, potentially compromising the injectivity and containment of CO_2 within geological formations. This limited knowledge, particularly during the early stages of a CCS project when reservoir data is scarce and data acquisition expensive, can significantly hinder informed decision-making (Oladyshkin et al., 2011; Pawar et al., 2015; Pawar et al., 2016). Moreover, in the early phase of CCS project development, operators typically have multiple potential storage sites in their portfolio, necessitating efficient screening methods to identify the most geologically suitable candidates. Therefore, the development of fast and efficient modeling tools for fault leakage assessment is crucial for CCS projects, guiding site selection, risk mitigation strategies, and long-term monitoring plans.

Reservoir simulation plays a vital role in quantifying potential fault leakage rates for large-scale CO_2 storage modeling. However, faults and damage zones are significantly smaller than the grid cells employed in typical field-scale simulations. While detailed models that incorporate complex fault geometries, rock properties, and multiphase flow dynamics can capture the interplay between CO_2 migration, leakage, and pressure changes, the computational demands associated with such models can be prohibitive (Jha and Juanes, 2014; Gasda et al., 2022; Snippe et al., 2022; Silva et al., 2023). This is especially true when considering uncertainties in subsurface data and the need for multiple simulations (scenario analyses) (Ringrose and Bentley, 2021). Sub-seismic faults, in particular, pose significant uncertainty due to the lack of detailed data and the computational burden of multiphysics forward modeling, which typically require weeks to run. To address these challenges, researchers have developed well-established simplification strategies that leverage two key characteristics of CO_2 storage systems: the strong buoyancy of CO_2 relative to brine and the significantly larger horizontal dimensions compared to the vertical dimension of the reservoir (Huppert and Woods, 1995; Yortsos, 1995; Nordbotten and Celia, 2011). These characteristics promote rapid CO_2 separation and vertical equilibrium within the reservoir. Vertical equilibrium (VE) flow models exploit this phenomenon by enabling the representation of the 3D reservoir system using a set of 2D governing equations, thereby significantly reducing computational costs.

Several CO_2 storage studies have demonstrated that VE simulations yield results comparable to those obtained from 3D simulations for benchmark and field-scale problems (Class et al., 2009; Nilsen et al., 2014; Bandilla et al., 2014; Nilsen et al., 2015; Nilsen et al., 2016; Moyner & Nilsen, 2019). The basic formulation of VE models assumes a sharp interface between CO_2 and brine and keeps the mathematical structure of the standard multi-phase Darcy equation. Hence, conventional simulators can be used. This very characteristic allows for their expansion to encompass a wider range of complex phenomena. Recent research has

successfully incorporated and evaluated various physical effects within VE models, including: 1) capillarity – the presence of non-negligible capillary pressure leads to the formation of a capillary fringe, a transition zone between the CO_2 and brine phases, rather than a sharp interface (Nordbotten & Dahle, 2011, Nilsen 2015); 2) residual trapping and hysteresis – these intrinsic properties of the rock can significantly influence the distribution and flow of fluids within the reservoir (Nordbotten & Celia, 2011; Doster et al., 2012; Doster et al., 2013; Du Plessis et al., 2013 Nilsen et al., 2016); 3) dissolution of CO_2 into reservoir brine (Gasda et al., 2011; Nilsen et al., 2016); 4) compressibility of CO_2 in the vertical extent (Anderson et al., 2015); 5) thermal effects (Gasda et al., 2013); 6) simplified geomechanics (Bjornara et al., 2016; Anderson et al., 2016, 2017); 7) Hybrid-VE – using a coupled approach of mixing 3D and VE models which can help with simulating near-wellbore effects and multilayer reservoir modeling (Moyner & Nilsen., 2019; Becker et al., 2017, 2018, 2022).

The objective of this paper is to couple a fault leakage function, which incorporates the fault properties and the vertical flow effects, with a VE reservoir model to facilitate computationally efficient CO_2 storage simulations. We employ a VE flow model implemented within the open-source software package MRST-co2lab, which is a module within the MATLAB Reservoir Simulation Toolkit (MRST) (Anderson, 2017; Lie, 2019). The fault is conceptualized as an increased vertical permeability through the caprock (due to the fracture network in the damage zone) while the horizontal permeability is reduced (due to throw and the presence of the fault core). Leakage rates are estimated using Darcy's law, considering the pressure differential across the layers connected by the fault. The flow is modelled as vertical single-phase flow along the fault. This simplification allows for a one-dimensional leakage system which lowers the cost of computation. The mathematical formulation of the proposed model is presented in section 2 and the results are discussed in section 3. This approach offers a cost-effective and efficient method for screening fault leakage risk during CO_2 injection and

storage, thereby contributing to ensuring safe and effective carbon storage. Furthermore, this methodology facilitates a more robust evaluation of storage potential while accounting for the inherent complexities and uncertainties associated with faulted geological settings.

2 Methods

This study examines the potential for carbon dioxide (CO_2) storage within a faulted reservoir (Figure 1). We employ a vertically integrated numerical model for reservoir-scale flow coupled with an analytical model for fault leakage. A brief overview of the governing equations used in these models is presented in this section.

2.1 Vertical Equilibrium Modelling

The VE modeling approach for CO_2 storage is a simplification of traditional reservoir simulation methods that is particularly useful for large-scale CO_2 storage projects. This approach hinges on the assumption of VE, which posits that the buoyancy forces acting on the CO_2 cause it to segregate vertically much faster than it can migrate laterally. As a result, the CO_2 forms a thin layer beneath the caprock or under intermediate sealing layers, and the vertical pressure and fluid saturation distributions can be approximated by buoyancy and capillary forces. VE models reduce the dimensionality of the problem by vertically averaging the governing equations, which include conservation of mass and Darcy's law for fluid flow through porous media. This simplification results in a model that requires fewer grid cells and is computationally less intensive compared to full three-dimensional simulations. Post-simulation, the vertical pressure and fluid saturations can be reconstructed from the set of upscaled variables obtained by vertically integrating the conservation equations. Figure 2 illustrates the typical compression and reconstruction steps during a VE simulation at early and late times for an example simulation problem. This section provides a concise review of

established equations for modeling flow in porous media and the VE simplification approach. For a more general and in-depth treatment of the derivations and the limits of the VE assumption, we refer the reader to the relevant literature (Yortsos 1995; Nordbotten & Celia, 2011;).

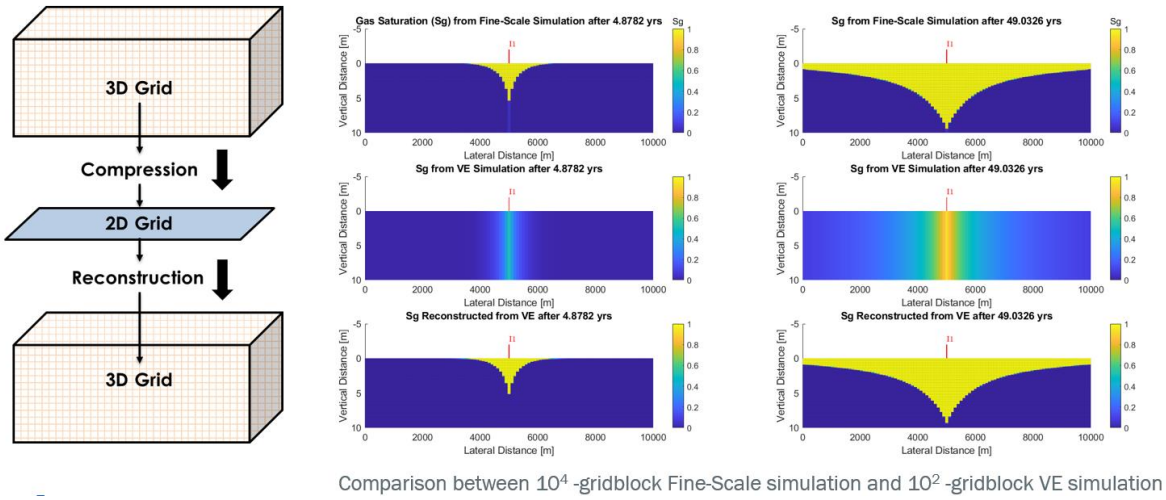

Figure 2 – Illustrative representation of the concept of VE model compression and reconstruction in a CO_2 injection simulation. The top panel shows an illustrative representation of the 3D simulation grid. The middle panel depicts the corresponding 2D grid generated by VE compression. The bottom panel presents the reconstructed 3D simulation grid obtained by solving the 2D VE model equations. These panels represent the grid configuration at both early and late stages of the CO_2 injection simulation. In this example, the VE compression reduces a 10^4-cell 3D grid to a 10^2-cell VE grid, achieving significant computational efficiency without substantial information loss.

Consider the three-dimensional mass conservation equation for two immiscible and incompressible fluid phases α, CO_2 ($\alpha = g$) and brine ($\alpha = w$) as

$$\frac{\partial(\phi s_\alpha)}{\partial t} + \nabla \cdot u_\alpha = q_\alpha, \tag{1}$$

where ϕ is the porosity, s_α is the saturation of phase α, u_α is the Darcy velocity of phase α, and q_α is a source/sink term in units of volume of phase α per time. The porous medium is assumed to be a rigid medium under isothermal conditions. The volume balance is established by

$$s_g + s_w = 1. \quad (2)$$

The Darcy velocity is given by

$$\boldsymbol{u}_\alpha = -\frac{k_{r\alpha}}{\mu_\alpha}\boldsymbol{k}(\nabla p_\alpha - \rho_\alpha \boldsymbol{g}), \quad (3)$$

where μ_α is the viscosity of phase α, $k_{r\alpha}$ is the relative permeability of phase α, $\boldsymbol{k}$ is the permeability tensor, p_α is the fluid pressure of phase α, ρ_α is the density of phase α, and $\boldsymbol{g}$ is the gravity acceleration vector. The phase pressures are related by the capillary pressure function

$$p_c = p_g - p_w. \quad (4)$$

Additional assumptions are that the capillary pressure and relative permeability can be represented by algebraic functions. These functions solely depend on saturation and its history. Equations (1) to (4) form a set of 10 equations with 10 unknowns that need to be solved for in three dimensions. The fluid saturation distributions and pressures are obtained by solving this system, provided that: 1) specific functions are chosen to represent relative permeability and capillary pressure, 2) initial conditions for pressure and saturation throughout the reservoir are provided, and 3) appropriate boundary conditions are specified along the edges of the reservoir model.

In subsurface flow processes, the lateral dimension of interest is typically orders of magnitude larger (hundreds of meters to kilometers) compared to the vertical dimension (meters to tens of meters). This disparity leads to a more rapid redistribution of fluids vertically, allowing for the approximation of VE (Nordbotten & Celia, 2011; Nordbotten & Dahle, 2011). Consider the reservoir domain to be bounded by impermeable, horizontally oriented layers with a constant uniform thickness H. The two fluids (brine and CO_2) are separated by a sharp interface within this reservoir. A cartesian coordinate system is employed, with the z-axis oriented in opposition to the gravitational vector (positive z upwards). Furthermore, for

simplicity in the presentation here, constant permeability and porosity are assumed within the vertical direction, though VE is not limited to those assumptions (Nordbotten & Celia 2012).

This vertical integration seeks to establish governing equations for the horizontal plane that utilize variables representing the average behavior throughout the reservoir thickness. Fine-scale quantities capture the variations within the vertical dimension, while coarse-scale quantities represent the horizontally averaged behavior. Under the assumption of vertical hydrostatic equilibrium, Equation (3) indicates that the pressure gradient in each phase balances the gravity ($u_{\alpha z} = 0$). This characteristic allows for the determination of pressure at any vertical position by integrating the pressure from a reference level. To facilitate analysis, we normalize the z-axis with respect to the reservoir height H. Here, $z = 0$ is assigned to the bottom and $z = 1$ to the top of the reservoir. Consequently, the top of the reservoir is chosen as the reference position for pressure integration as

$$P_\alpha = p_\alpha(z = 1). \tag{5}$$

The reconstructed pressure is then given as

$$p_\alpha(z) = P_\alpha + \rho_\alpha g H(1 - z). \tag{6}$$

The other coarse-scale quantities are introduced by integrating the fine-scale quantities. This is done under the assumption of a homogeneous system with isothermal and incompressible fluid. We can obtain the coarse-scale equivalents after normalizing the vertical axis to the reservoir height and writing the equations in dimensionless form. For such systems, the coarse-scale equivalents of porosity Φ, permeability K, and viscosity M_α are simply a product of their respective fine-scale counterparts with reservoir height. This is because the averaging or integration process does not introduce any scaling factors in this case. The spatially dependent quantities are given as

$$S_\alpha = \frac{H}{\Phi} \int_0^1 \phi s_\alpha dz, \tag{7}$$

$$U_\alpha = H \int_0^1 u_{\alpha||} dz, \tag{8}$$

$$K_{r\alpha} = \frac{H}{K} \int_0^1 k_{||} k_{r\alpha}\big(s_\alpha(z)\big) dz. \tag{9}$$

The subscript || denotes the variables in horizontal components such that U_α is a two-dimensional vector instead of three dimensions. With these definitions, Equations (1) to (4) after integrating over the vertical extent are given as

$$\frac{\partial(\Phi S_\alpha)}{\partial t} + \nabla_{||} \cdot (U_\alpha) = Q_\alpha, \tag{10}$$

$$S_g + S_w = 1, \tag{11}$$

$$U_\alpha = -K \frac{K_{r\alpha}}{M_\alpha} \nabla_{||} \mathrm{P}_\alpha, \tag{12}$$

$$P_c(\cdot) = P_g - P_w, \tag{13}$$

where (•) is used to highlight the upscaled dependence of the capillary pressure function that is yet to be determined. Equation (9) demonstrates that reconstructing the vertical, fine-scale saturation distributions, $s_w(z;\ x, y)$, is necessary to determine the effective parameter functions employed in a purely coarse-scale model. Fortunately, the assumption of hydrostatic fluid distribution facilitates this reconstruction process. By examining Equation (6), we observe that the fine-scale capillary pressure, $p_c(z;\ x, y)$, must compensate for the buoyancy force arising from the density difference. This relationship allows for the construction of the fine-scale capillary pressure and its subsequent connection to the coarse-scale capillary pressure as

$$p_c(z;\ x, y) = P_c(x, y) - \big(\rho_w - \rho_g\big) g H (1 - z). \tag{14}$$

A well-defined relationship between capillary pressure and water saturation enables the establishment of invertible $p_c - s_w$ mappings. These mappings allow for the reconstruction of the vertical saturation distribution, $s_w(z;\ x, y)$, given a specific coarse-scale capillary pressure P_c. Furthermore, Equation (7) can be employed to obtain a $P_c - S_w$ relationship. By leveraging

this relationship, the fine-scale saturation distribution $s_w(z;\, x, y)$ is determined for a given coarse-scale saturation S_w. Consequently, coarse-scale relative permeabilities $K_{r\alpha}$ are dependent on coarse-scale saturations only.

2.2 Fault Leakage Function

This section details the steady-state analytical solution used to estimate leakage rates along the fault. The fault is conceptualized to connect the storage reservoir with a secondary aquifer at a shallower depth, which acts as sink for the leaking CO_2. Only faults of shorter lengths such that the CO_2 fluid properties remain nearly constant are considered here, while the long-range fault leakage (faults that connect the reservoir to the surface or seafloor) with variable CO_2 fluid properties and decompressive cooling has been investigated previously (Pruess, 2011; Ramachandran et al., 2017). The leaky fault is conceptualized as consisting of a low-conductivity (i.e., low permeability) core that prevents flow across the fault. This core is surrounded by two high-conductivity (i.e., high-permeability) damage zones that permit flow vertically along the fault as shown in Figure 3 (Faulkner et al., 2010). This damage zone is referred to here as "the fault zone" or simply "the fault", and the low-conductivity core is represented as a no-flow boundary in the model. Hence the fault leakage will predominantly occur along the damage zone which is hypothesized as an equivalent porous medium with appropriate rock properties describing it. Estimating the hydraulic properties of the fault, particularly within the fault core and damage zone, is crucial for accurately modeling fault leakage. While insights can be gained from studying outcrop analogues, inherent uncertainties remain at the finer scale. Several researchers have developed stochastic modeling approaches to predict the fault properties, such as permeability, among other parameters (Berge et al., 2022; Gasda et al., 2022; Salo-Salgado et al., 2023; Rizzo et al., 2024). However, for this specific model, we are assuming constant fault properties throughout the simulation. The flow along the

fault is described using Darcy's law by considering the pressure differential across the storage reservoir and the secondary aquifer, and the flow is assumed to occur only in the vertical direction. Once the CO_2 plume reaches the base of the fault within the aquifer, it is hypothesized to form a thick layer, acting as a barrier for aqueous phase entry into the fault (Kang et al., 2014). As a result, the aqueous phase flux along the fault is considered negligible and excluded from the model.

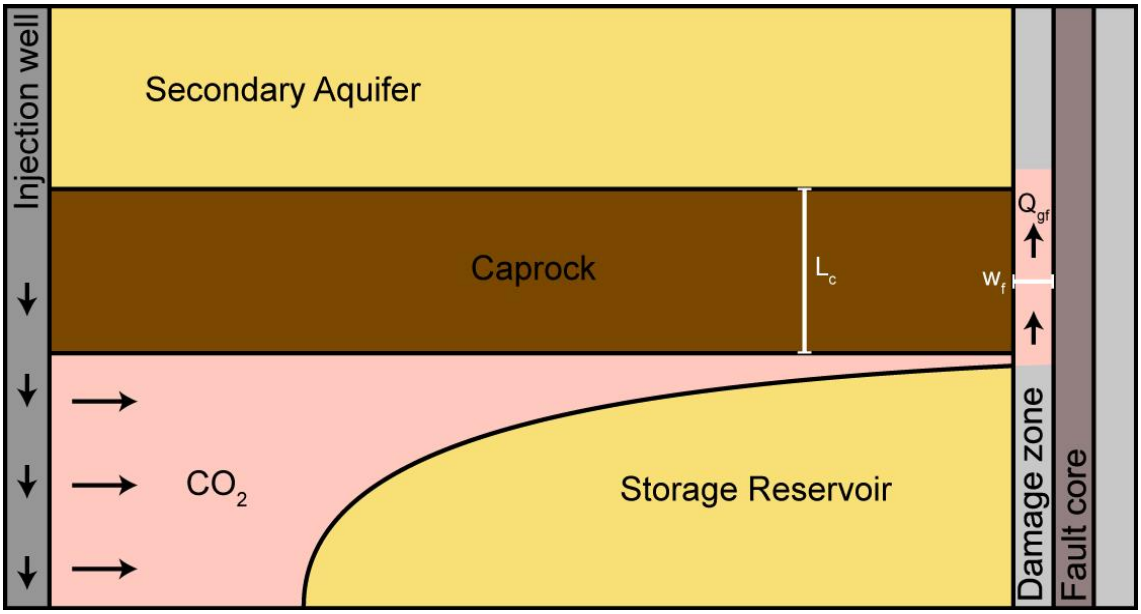

Figure 3 – A schematic representation of a vertical cross section of a storage reservoir containing a fault (gray). The black line represents the interface between CO_2 and the brine phase. CO_2 leaks along the damage zone of the fault once it reaches the base of the fault within the reservoir.

Several researchers have indicated that the CO_2 needs to overcome the capillary entry pressure of the fault, commonly referred to as the fault displacement pressure, for it to leak (Espinoza et al., 2017; Zheng & Espinoza, 2022). This capillary entry pressure is controlled by an effective aperture of the fracture network and as such strongly depends on the geomechanical properties of the fault as well as the pressurization of the target reservoir. For simplicity, we keep this parameter constant here. We base the flux calculation on the model presented by Neufeld et al. (2009), with slight modifications to account for the reservoir overpressure caused

by injection. This model describes leakage through fissures between two aquifers, with one being the targeted CO_2 storage site. We model the driving potentials ψ as

$$\psi = \Delta\rho g h_g + (P_w - P_{w0}) - p_e, \tag{15}$$

where $\Delta\rho = \rho_w - \rho_g$ is the density difference between brine and CO_2, h_g is the height of CO_2 which is obtained from the coarse-scale gas saturation S_g (after accounting for the reservoir rock-fluid characteristics), of the reservoir block connected to the fault block, P_w is the brine pressure in the reservoir, P_{w0} is the initial brine pressure in the reservoir, and p_e is the capillary entry pressure of the fault/fractures. The vertical gas leakage flux Q_{gf} along the fault is given as

$$Q_{gf} = \begin{cases} 0, & \psi \le 0 \\ \dfrac{A_f k_f}{\mu_g} \dfrac{(\psi + \Delta\rho g L_c)}{L_c}, & \psi > 0 \end{cases} \tag{16}$$

where A_f is the area of the fault perpendicular to flow, k_f is the vertical fault permeability and L_c is length of the caprock or the length of the fault connecting the reservoir to the secondary aquifer. This formulation accounts for the capillary entry pressure required for CO_2 to enter the fault. This approach relaxes the assumption of VE at the grid block where the fault is connected, allowing for non-zero vertical flow. However, for steady state single phase flow, fault leakage does not have a significant effect on reservoir predictions (Kang et al., 2014). By incorporating these key factors, the model aims to provide a more realistic representation of the fault leakage process.

2.3 Model Implementation

The leakage along the fault is numerically simulated as a fault leakage function, which is represented as a source/sink term in the material balance equations (Equation 10). This methodology circumvents the explicit discretization of faults, thereby capturing their impact on fluid flow and replicating their influence without requiring a computationally intensive, fully

discretized fault representation. The fault leakage function is related implicitly to the primary unknowns of the reservoir model using the gas saturation and the overpressure terms of the grid blocks adjacent to the fault. The flow rate at the fault-reservoir interface is represented as shown in Equation 16. From a simulation perspective, fault leakage occurs when the leakage constraint, expressed as $\Delta\rho g h_g + (P_w - P_{w0})$, exceeds the fault capillary entry pressure p_e and the upscaled gas saturation is greater than zero. However, numerical experiments have demonstrated that this criterion can result in unstable behaviour, characterized by frequent fluctuations (appearance and disappearance of the fault leakage term) during the iteration process and between time steps, which causes convergence issues and increases simulation time. To address this problem, the implementation of a smoothing function for the leakage rate term enables the adoption of a more robust fault leakage function. We use a smoothing function, such that $\hat{Q}_{gf} = Q_{gf} f(\psi)$ with the smoothing function $f(\psi) = \left(1 - e^{(-\xi\,\psi)}\right)$ and the smooting parameter ξ. In our simulations we use $\xi = 10^{-3}\ Pa^{-1}$ to regulate the fault leakage rate upon the initial occurrence of a non-zero fault leakage term. Under rigorous consideration, permitting the leakage constraint to marginally exceed p_e without initiating fault leakage introduces a minor inaccuracy in leakage rates. However, this approach has a negligible impact on long-term simulation results while significantly improving the efficiency of the simulations with respect to timesteps and convergence. The fault permeability assigned to the fault leakage term represents the combined effect of the fault core permeability and the surrounding damage zone permeability. This combined parameterization simplifies the model while preserving the essential flow characteristics associated with the fault system. The resulting reservoir is discretized based on a finite volume discretization using the two-point flux approximation method, as implemented in the MRST (Lie, 2019) framework.

3 Results and Discussion

In this section, we present the results obtained from applying the fault leakage function coupled with the VE reservoir model to several CO_2 injection scenarios.

3.1 Test case – comparison with 2D simulations

The test case presented in this section are designed to validate the fault leakage modeling methods presented in section 2. A 2D two-phase numerical model is used to simulate the fault leakage rates within the simplified CO_2 storage setting (Figure 4a). The objective of this test case is to compare the fault leakage rates between the 2D numerical simulation with an explicit representation of the fault and the VE model with the fault leakage function proposed in this work. The test case simulates fluid flow through a conceptual model comprising two horizontal aquifers separated by a caprock and connected by a vertical, conductive fault. The bottom aquifer serves as the storage reservoir, while the top aquifer is the top reservoir. The fault is treated as an equivalent porous medium with the reservoir, fault, fluid, and rock-fluid properties as specified in Table 1. Although the permeability of the aquifers and faults is simplified for comparative purposes, it is crucial to emphasize that the primary focus is on the interaction of these components, rather than precise geological representation. We expect that varying these parameters within reasonable bounds would not significantly alter the leakage rate comparison.

A numerical grid of 12,000 cells discretizes the system with a resolution of 1 m x 1 m x 0.25 m (x, y, and z directions, respectively), resulting in a physical model with dimensions of 100 m x 30 m, consisting of three layers, each 10 m thick. The fault zone, located on the right side of the model, is 5 m wide and 10 m long. The system is assumed to be in hydrostatic equilibrium with 100% water saturation initially, and the relative permeability is governed by the Brooks-Corey model with parameters described in Table 1. No-flow boundaries are assumed at the top, bottom, and the right side (representing the no flow across the fault core).

The left boundary is treated as an open boundary with the pressure maintained as hydrostatic. The system is initialized with a constant CO_2 column height at the left boundary of the storage reservoir. This column height and the boundary pressures can be varied to simulate buoyancy-driven and pressure-driven conditions, allowing for a comprehensive evaluation of the fault leakage modeling approach.

Table 1 – Summary of model parameters used for fault leakage function validation simulation described in section 3.1.

Property	**Value**
Bottom Reservoir and Top Reservoir Properties	
Top reservoir porosity	0.3
Bottom reservoir porosity	0.3
Top reservoir permeability (D)	10
Bottom reservoir permeability (D)	10
Reservoir overpressure (bars) (case 2 and 3)	1
Caprock properties	
Caprock permeability (mD)	1×10^{-6}
Caprock porosity	0.3
Fault properties	
Fault porosity	0.03
Fault permeability (mD)	1
Fault width (m)	5
Fault length (m)	10
Fault capillary entry pressure (bars) (case 3)	0.5
Bottom Reservoir, Fault and Top Reservoir Relative Permeability Properties	
Residual gas saturation	0
Residual brine saturation	0
Gas end-point relative permeability	1
Brine end-point relative permeability	1
Gas relative permeability exponent	1
Brine relative permeability exponent	1
Fluid properties	
Gas density (kgm^{-3})	500
Brine density (kgm^{-3})	1000
Gas viscosity (Pa.s)	0.5×10^{-6}
Brine viscosity (Pa.s)	0.9×10^{-5}

Three specific parametrizations are considered to compare the performance of the fault leakage modeling approach, 1) The reservoir and boundary pressures is hydrostatic. The pressure of the CO_2 column is derived solely from density differences, and the flow is driven

by buoyancy. This parametrization mimics the migration phase of CO_2 storage. 2) The reservoir pressure is hydrostatic, but the boundary pressure is elevated to mimic the typical pressure increase observed during injection. The pressure of the CO_2 column is derived from both, the density differences, and the pressure elevation. 3) Similar to Case 2, the third scenario contains an additional capillary entry pressure for the fault, which acts as a pressure barrier that the CO_2 must exceed to enter the fault zone. The 2D numerical simulation are run to steady-state conditions for each of the three cases. The leakage rate, specified as the flow leaving from the top of the fault, is then compared to the leakage rate obtained from the VE model with the fault leakage function (Figure 4b). The proposed fault leakage function compares well with the numerical simulations for all the three scenarios considered in this test case and demonstrates that it is robust and suitable for capturing the key factors influencing fault-related CO_2 leakage, i.e., buoyancy, pressure gradients, and capillary entry pressure. Moreover, the model's computational efficiency is improved by bypassing the explicit representation of the fault and top reservoir. This validation gives confidence that our model can be applied to field-scale CO_2 storage simulations.

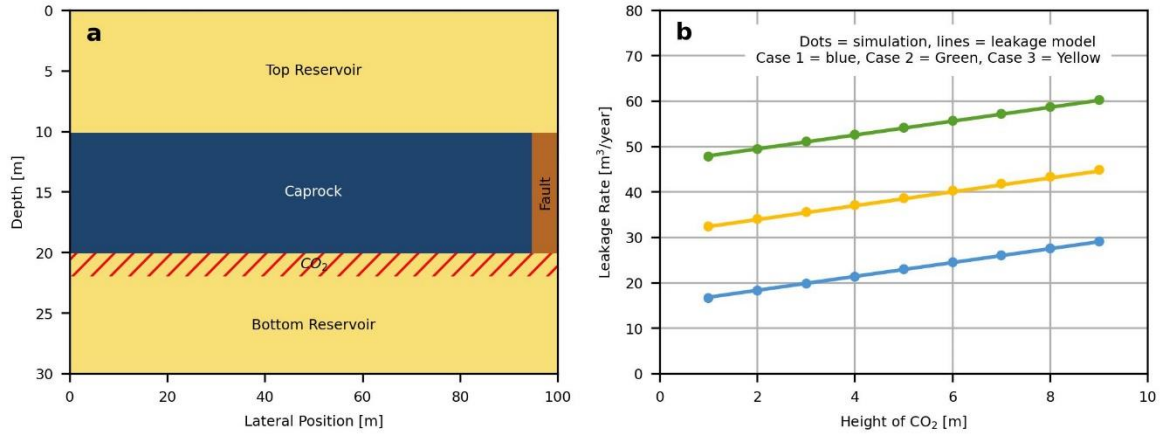

Figure 4 –Grid representation of 2-D fine scale simulation (a) and fault leakage rate comparison between numerical simulation and VE model with fault leakage function (b). The three cases

considered are: (1) hydrostatic reservoir and boundary pressure, (2) elevated reservoir boundary pressure, and (3) fault capillary entry pressure.

It is important to highlight the potential limitations of the steady-state, single-phase fault leakage assumption used in our modeling approach. For instance, in the overpressure parametrization (2) with a 5-meter CO_2 column height, the calculated leakage rate is 53 m^3 per year. Accounting for the fault dimensions, this corresponds to a CO_2 Darcy flux of 0.03 m per day. This implies that it takes approximately 344 days (~1 year), for the CO_2 to travel the 10-meter distance separating the bottom reservoir and the top reservoir. Although faults are typically characterized by very low porosity, and the impact of CO_2 accumulation within the fault on the leakage rate may be minimal (Faulkner et al., 2010; Caine et al., 1996), there remains a significant delay in reaching the top reservoir that is not captured because the current approach presupposes instantaneous leakage once the CO_2 reaches the base of the fault. This raises a pertinent question regarding the definition of leakage - whether it occurs once CO_2 enters the top reservoir or once it enters the fault from the bottom reservoir. However, the current modeling approach does not explicitly account for these dynamic effects during the fault leakage process. While acknowledging these limitations is crucial, it is equally important to contextualize the scale of typical CO_2 storage simulations, which extend from few decades to few centuries. Within this broader temporal framework, the steady-state, single-phase assumption may offer a reasonable approximation that allows us to screen leakage rates across a broad range of possible reservoir scenarios before commencing more detailed simulation studies that capture the full physics of fault leakage in a specific reservoir scenario. This consideration underscores the necessity of balancing model complexity with computational feasibility, particularly in the context of large-scale, long-term CO_2 storage simulations.

3.2 Test case – convergence analysis

The following test case aims to elucidate the impact of grid resolution and time step size on the fault leakage modeling methods presented in Section 2. A 2D, two-phase numerical model is employed to simulate fault leakage rates within a simplified CO_2 storage setting (x 5a). This test case, with minor modifications, is based on the scenario described in Section 3.1. It simulates fluid flow through a geological model consisting of a horizontal aquifer located beneath a faulted seal. The aquifer serves as the storage reservoir, and the faulted seal is treated as an equivalent porous medium. The properties of the reservoir, fault, fluid, and rock-fluid interactions are specified in Table 2. While the physical dimensions of the aquifer are 100 m by 10 m, and the fault zone is also 100 m wide and 10 m long, are simplified for convergence analysis, it is important to note that the primary focus is on the interplay of these components without being constrained by precise geological representation. We expect that varying these dimensions within reasonable bounds would not significantly alter the observed convergence behavior. The system is assumed to be in hydrostatic equilibrium with an initial water saturation of 100%. Relative permeability is governed by the Brooks-Corey model, with parameters detailed in Table 2. No-flow boundaries are assumed at the bottom, while the left and right boundaries are treated as open, with pressure maintained as hydrostatic. The system is initialized with a constant CO_2 column height of 5 m at the left boundary of the storage reservoir. This column height and the boundary pressures can be varied to simulate buoyancy-driven and pressure-driven conditions, similar to those in Section 3.1. The grid blocks enclosing the faulted is modified to incorporate the fault leakage function, with properties mentioned in Table 2, to mimic along-fault leakage.

Table 2 – Summary of model parameters used for convergence analysis simulation described in section 3.2.

Property	**Value**
Reservoir Properties	

Reservoir porosity	0.3
Reservoir permeability (mD)	100
Faulted seal properties	
Fault porosity	0.03
Fault permeability (mD)	1×10^{-3}
Fault length (m)	10
Reservoir and Fault Relative Permeability Properties	
Residual gas saturation	0
Residual brine saturation	0
Gas end-point relative permeability	1
Brine end-point relative permeability	1
Gas relative permeability exponent	1
Brine relative permeability exponent	1
Fluid properties	
Gas density (kgm^{-3})	500
Brine density (kgm^{-3})	1000
Gas viscosity (Pa.s)	0.5×10^{-6}
Brine viscosity (Pa.s)	0.9×10^{-5}

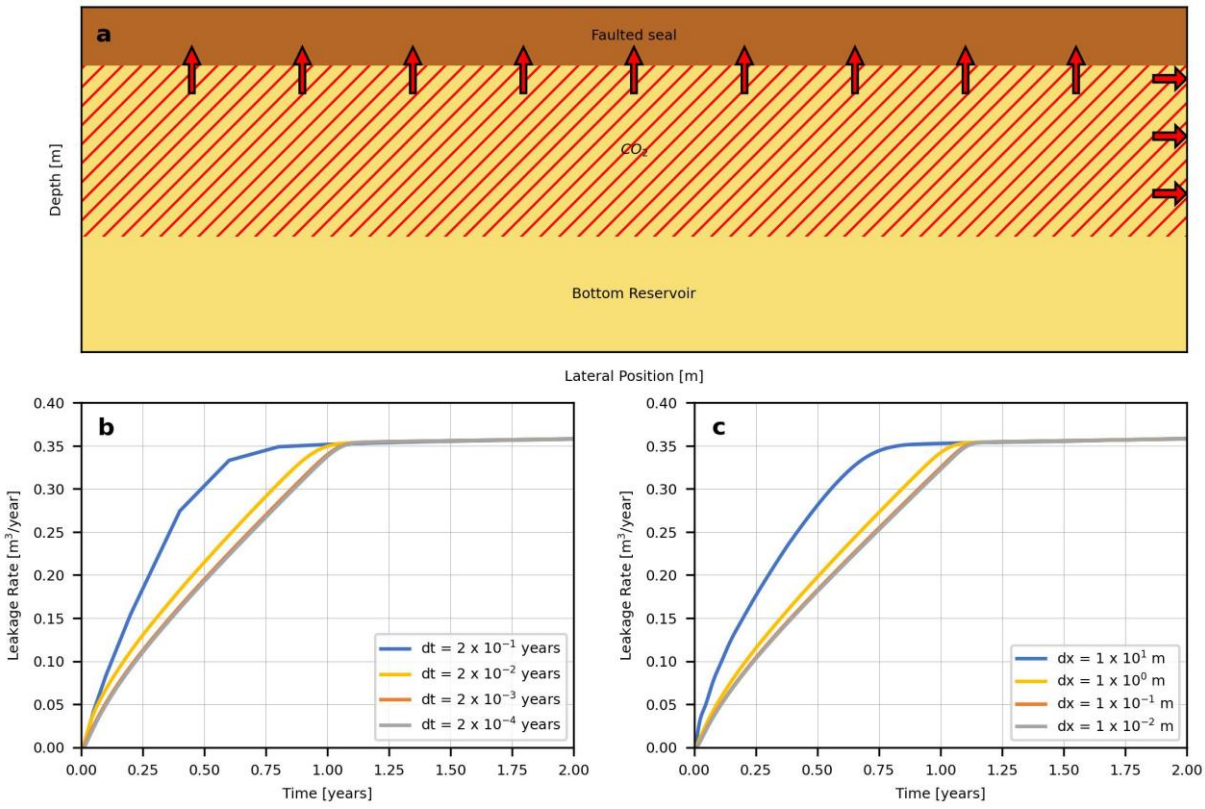

Figure 5 – Grid representation of VE simulation setup of CO_2 storage with a faulted seal to assess the impact of grid block dimensions and time step size on fault leakage modeling (a), fault leakage rate comparison for varying time step sizes for a constant grid block dimension of

1 m (b) and fault leakage rate comparison for varying gridblock dimensions at a time step of 4 x 10^{-3} years (c).

Figure 5b illustrates the leakage rate for two years with time steps varying from 2 x 10^{-1} years to 2 x 10^{-4} years and a grid block dimension of 1 m. Figure 5c illustrates the leakage rate for two years with grid block dimensions varying from 1 x 10^{1} m to 1 x 10^{-2} m and a time step of 4 x 10^{-3} years. A key observation is that the leakage rate converges towards a consistent solution for both, time and space. Coarser grids and larger time steps lead to overestimated leakage rates in the first year. Subsequently, all time steps and grid block sizes converge toward the same leakage rate predictions. While the total leakage increases with larger time steps and grid sizes, the magnitude of this increase becomes negligible after 100 years of simulation (when the system reaches steady state). For instance, the total leakage after 100 years is only 0.0025% higher for the 2 x 10^{-1} year time step compared to the 2 x 10^{-3} year time step, and 0.0027% higher for the 1 x 10^{1} m grid size compared to the 1 x 10^{-2} m grid size. Resizing grid blocks proportionally resizes the fault leakage function, ensuring the total fault width remains constant. Consequently, the number of fault leakage terms increases with a higher number of grid blocks. Despite this increase, the impact on total leakage predictions remains relatively low. It is important to acknowledge that this model uses a fault leakage function instead of explicitly representing the faults, to ensure computational efficiency. Despite this simplification, the model is able to approximate the reservoir behavior and leakage rates outcomes with sufficient reliability. This approach facilitates the rapid screening of potential storage sites, enabling the identification of promising candidates. Consequently, resources can be strategically allocated to design comprehensive data acquisition campaigns tailored to the specific geological complexities of selected sites. By expediting the early screening phase, this methodology contributes to the overall acceleration of CO_2 storage project development in geologically complex settings.

3.3 Sloping reservoir with a leaky fault

The case presented in this section is designed to test the fault leakage function for a gently sloping reservoir with a large fault. The conceptual model comprising of a gently sloping reservoir connected to a secondary aquifer by a fault is shown in Figure 6a. The reservoir is discretized as a VE grid with 2500 cells, each measuring 20 m x 20 m in the x and y directions, respectively, resulting in a physical model with dimensions of 1000 m x 1000 m. The reservoir has a thickness of 10 m and a slope of ~3 degrees. The fault is treated as an equivalent porous medium using the fault function, and the reservoir, fault, fluid, and rock-fluid properties as specified in Table 3. The system is assumed to be in hydrostatic equilibrium with 100% water saturation initially, and the relative permeability is governed by the Brooks-Corey model with parameters mentioned in Table 3. No-flow boundaries are assumed at the top, right and left boundaries. The bottom boundary is treated as an open boundary with the pressure maintained as hydrostatic. Hence this bottom boundary acts as a sink for the heavier brine phase and allows for up-dip movement of CO_2. Unlike previous simulations where the CO_2 injection was controlled by boundary conditions, this simulation uses the rate constrained well for CO_2 injection. The injection location is at the coordinate pair (100 m, 500 m) for an injection rate of 1229 tons per year over 3 years followed by 97 years of migration. The fault zone is located in the center of the model., i.e., 500 m away from either side boundary in x-direction. The fault is 800 m long in the y-direction. The grid blocks enclosing the fault are modified to 1) set the across-fault permeability to zero, mimicking an impermeable fault core, and 2) incorporate the fault leakage function with the properties mentioned in Table 3 to mimic along fault leakage. The goal of this case study is to analyze the evolution of CO_2 leakage rates and assess the impact of fault capillary entry pressure on these rates.

VE reservoir simulation is conducted with a time step of one year to evaluate the impact of the fault on the migration of a CO_2 plume within the reservoir. The evolution of the CO_2 plume is depicted at the end of the injection period (Figure 6b) and after 97 years of migration

(Figure 6c). The simulation results demonstrate the preferential up-dip movement of the CO_2 plume within the reservoir. Notably, significant quantities of CO_2 are observed to accumulate at the base of the fault since the impermeable fault core inhibited further across-fault migration within the reservoir. This leads to an increase in gas saturation down dip of the fault until the CO_2 plume migrated laterally to the fault tips, after which it continued its unhindered up-dip movement. Leakage along the fault occurs once the CO_2 reached the fault. The leakage rate reached its maximum and then reduced after the CO_2 migrated around the fault tips. After this point, continued upward migration reduced the amount of CO_2 trapped below the fault, consequently decreasing the leakage rates (Figure 6d). A total of 3680 tons of CO_2 is injected into the reservoir, of which 880 tons has leaked along the fault, accounting for approximately 24% of the injected CO_2.

Table 3 – Summary of model parameters used for the sloping reservoir simulation case described in section 3.3.

Property	**Value**
Reservoir description	
Number of cells (NX*NY)	50 x 50
Cell dimensions (DX*DY) (m)	20 x 20
Reservoir height (H) (m)	10
Reservoir slope (degrees)	2.86
Average reservoir depth (m)	975
Porosity	0.3
Permeability (mD)	100
Rock compressibility (Pa^{-1})	4.35×10^{-10}
Fluid properties (at 2000m depth)	
Brine viscosity (Pa.s)	3.13×10^{-4}
Gas viscosity (Pa.s)	3.21×10^{-5}
Brine density (kgm^{-3})	1001
Gas density (kgm^{-3})	389.7
Fault properties	
Fault permeability (mD)	1×10^{-3}
Fault width (m)	5
Fault length (m)	100
Rock-Fluid properties (Brooks-Corey Model)	
Residual gas saturation	0.2
Irreducible brine saturation	0.27
Gas end-point relative permeability	1

Brine end-point relative permeability	1
Gas relative permeability exponent	1
Brine relative permeability exponent	1

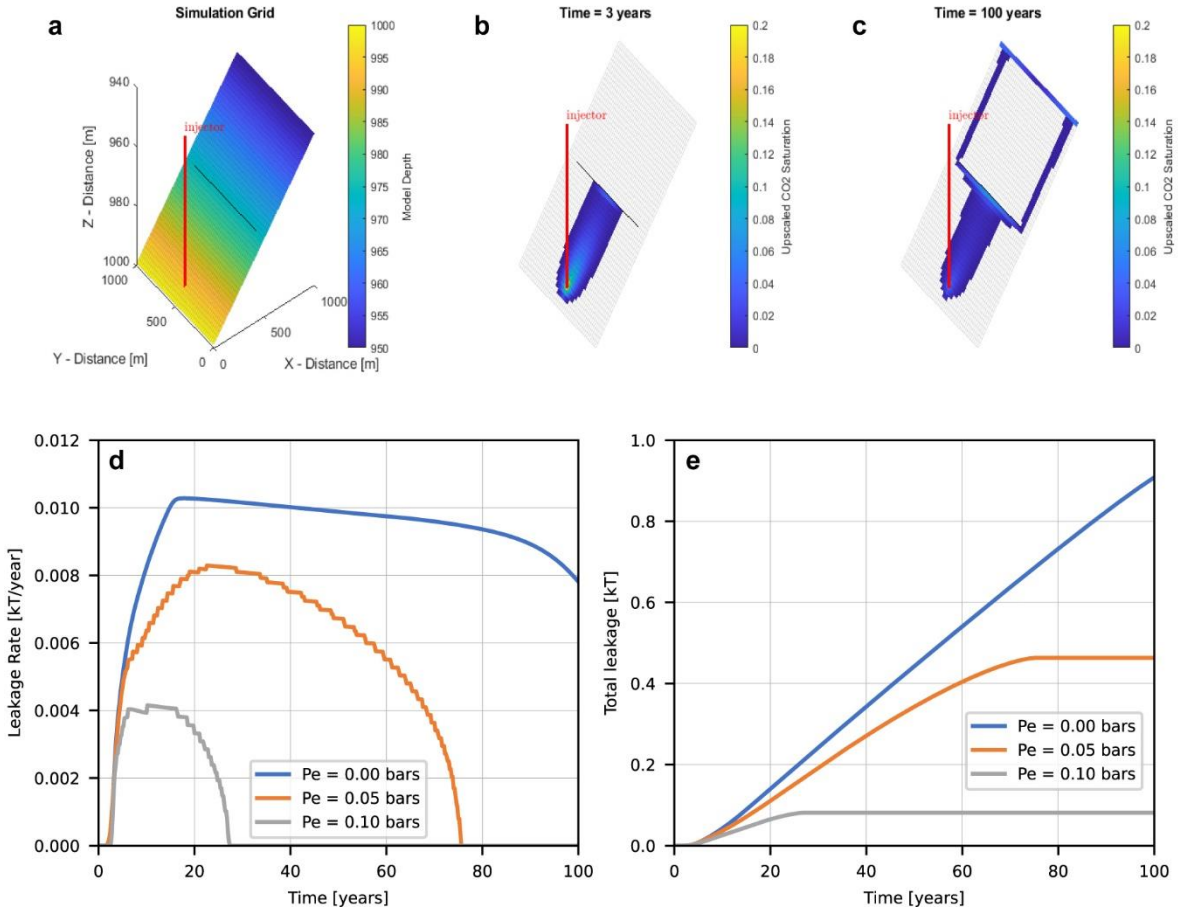

Figure 6 – Simulation of CO_2 plume migration in a sloping reservoir (note the slope is exaggerated) and leakage along a fault showing the inclined 3D-view of the reservoir and the location of the fault (a), the CO_2 plume saturation distribution at the end of the injection period (b) the CO_2 plume saturation distribution after 100 years of migration (c), the CO_2 leakage rates along the fault for different fault capillary entry pressures (d) and the cumulative CO_2 leakage after 100 years for different fault capillary entry pressures (e).

The introduction of a capillary entry pressure constraint for fault leakage reveals interesting leakage dynamics. Figure 6d depicts the leakage rates, while Figure 6e shows the cumulative leakage after 100 years for varying fault capillary entry pressures ranging from 0 to 0.1 bar. Both the maximum fault leakage rate and cumulative leakage decreases with the

increase in fault capillary entry pressure. The scenario with zero fault capillary entry pressure represents unconstrained leakage along the fault, allowing for continuous CO_2 leakage. In contrast, higher capillary entry pressures act as a barrier, limiting the extent of CO_2 migration and leakage through the fault zone. An important observation pertains to the leakage rate reaching zero. This occurs when the trapped CO_2 plume is unable to overcome the capillary entry pressure barrier, effectively stopping further leakage along the fault. The time at which leakage ceases decreases with the increase in fault capillary entry pressure, highlighting its potential for mitigating leakage.

3.4 Field-scale fault leakage quantification

The J area, a conceptual CO_2 storage site within the Malay Basin offshore Peninsular Malaysia, is used to illustrate the fault leakage function coupled with VE models for field-scale fault leakage quantification. The Malay Basin is approximately 500 km long, 200 km wide, and 12 km deep, situated in coastal waters less than 100 km from the east coast of Peninsular Malaysia (de Jonge-Anderson et al., 2024b). It is a mature hydrocarbon basin with over 181 discoveries since and over 14.8 billion barrels of oil equivalent in recoverable resources since 1981 (Madon, 2021). Recently, it has been considered an important area for CCS (Abd Rahman et al., 2022; Hasbollah et al., 2020) due to its numerous mature fields that could be repurposed, providing an abundance of data and production history. Saline aquifers offer great potential, however, limited data and understanding necessitate uncertainty assessment and screening analysis to determine storage traps.

The J area lies on the northern margin of the basin, 50 km from the nearest hydrocarbon field with the target reservoir situated at 1984 m depth below the seafloor. The main storage interval consists of a thick and heterogeneous sequence of lower to middle Miocene sandstones, mudstones, and coals, with the sandstones representing the target reservoir. The 3D reservoir

grid, depths, petrophysical and reservoir properties are obtained from de Jonge-Anderson et al. (2024a, 2024b). The relevant reservoir properties are summarized in Table 4. Previous storage capacity assessment for this site have identified the best injection location at the coordinate pair (413100 m, 718500 m) (UTM 48 N – reference coordinate system) for an injection rate of 1 MT per year over 30 years followed by 970 years of migration (de Jonge-Anderson et al., 2024b), assuming no leakage through the caprock. The top of the reservoir lies at depths between 1500 m and 2500 m below a seafloor depth of 70 m. The reservoir pressure is assumed hydrostatic with a temperature profile following a geothermal gradient of 50°C/km and a seafloor temperature of 24°C (Madon & Jong, 2021). A 26 km-long fault is introduced into this grid as shown in Figure 6a and the fault properties are provided in Table 4. The injection well is located 12 km away from the fault. The grid blocks enclosing the fault are modified to 1) set the across-fault permeability to zero, mimicking an impermeable fault core and 2) incorporate the fault leakage function with the properties mentioned in Table 4 to simulate along fault leakage. The model boundaries are treated as open, with the pressure maintained at hydrostatic conditions. The goal of this case study is to understand the impact of fault leakage on the injection rate and storage capacity within the J area.

Table 4 – Summary of model parameters used for field-scale fault leakage quantification simulation case described in section 3.4 (Adapted from (de Jonge-Anderson et al., 2024b))

Property	**Value**
Reservoir description	
Number of cells (NX*NY*NZ)	100 x 110 x 5
Cell dimensions (DX*DY) (m)	200 x 200
Area (km^2)	440 (22 x 20)
Average top reservoir depth (m)	1984
Porosity	0.05 – 0.25 (arithmetic mean = 0.145)
Permeability (mD)	1.2 –241 (arithmetic mean = 39.4)
Rock compressibility (Pa^{-1})	4.35×10^{-10}
Seafloor temperature (°C)	24
Temperature gradient ($°Ckm^{-1}$)	50
Seafloor Depth (m)	70
Fluid properties (at 2000m depth)	
Brine viscosity (Pa.s)	3.13×10^{-4}

Gas viscosity (Pa.s)	3.21×10^{-5}
Brine density (kgm^{-3})	1001
Gas density (kgm^{-3})	389.7
Fault properties	
Fault permeability (mD)	1×10^{-3}
Fault width (m)	5
Fault length (m)	500
Rock-Fluid properties (Brooks-Corey Model)	
Residual gas saturation	0.2
Irreducible brine saturation	0.27
Gas end-point relative permeability	1
Brine end-point relative permeability	1
Gas relative permeability exponent	1
Brine relative permeability exponent	1

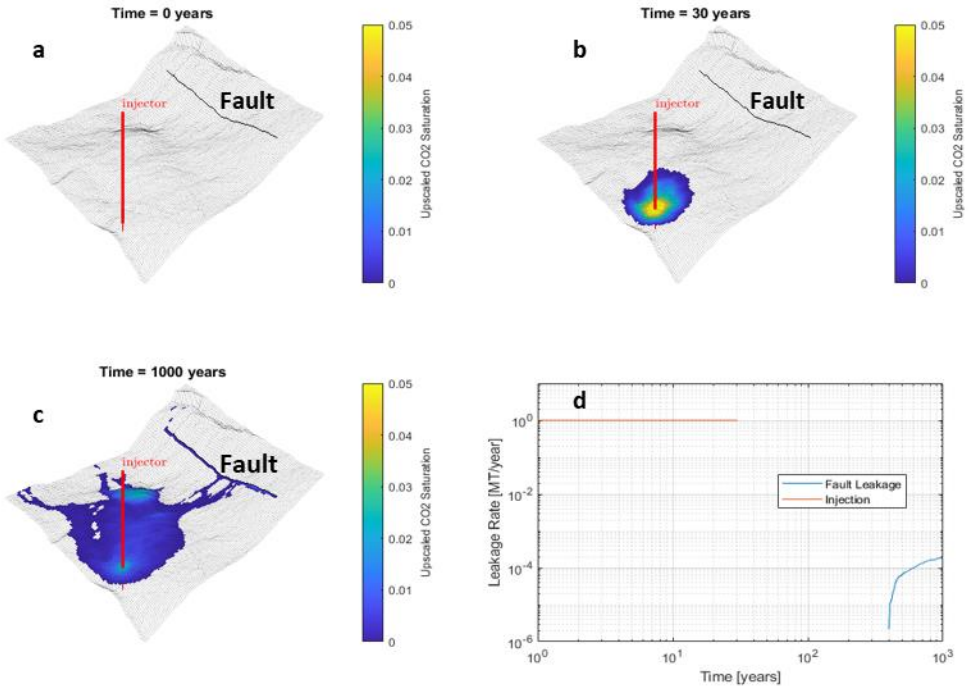

Figure 7 – Simulation of CO_2 plume migration and leakage along a leaky fault. Inclined 3D view of the reservoir showing the location of the fault (a), CO_2 plume saturation distribution at the end of the injection period (b), CO_2 plume saturation distribution after 1000 years of migration (c) and temporal evolution of the CO_2 leakage rate along the fault (d).

A numerical simulation is performed to assess the impact of a fault on the migration and leakage of a CO_2 injected into the reservoir (Figure 7a). The evolution of the CO_2 plume is

depicted at the end of the injection period (Figure 7b) and after 1000 years of the migration phase (Figure 7c). The simulation results show the CO_2 plume moving up-dip and accumulating within an anticline structure. Considerable amounts of CO_2 accumulate at the base of the fault, with the impermeable fault core preventing further migration across the fault. The CO_2 plume reaches the fault after approximately 400 years and immediately begins leaking through the fault (Figure 7d). The leakage rate increases as more of the migrating CO_2 became trapped at the faulted block representing the hanging wall. By the end of the 1,000-year simulation period, a total of 30 MT of CO_2 has been injected, of which 0.085 MT (0.28%) has leaked along the fault. These results highlight the impact that the presence of a fault can have on the migration and containment of a CO_2 plume in a storage setting and the ability to address this impact quickly as each simulation takes under 30 seconds on Apple MacBook Pro with the Apple M1 chip.

The fault permeability and the thickness of the damage zone play a crucial role in determining the magnitude of CO_2 leakage, as shown in Figure 8. While these parameters do not affect the onset of leakage (Figure 8a). The total amount of leakage decreases, following a power-law trend with an exponent of 0.9895 as the product of fault permeability and damage zone thickness $k_f w_f$ decreases (Figure 8b). While Equation 16 predicted an exponent of 1, the observed deviation suggests that variations in pressure buildup induced by fault permeability also influence leakage rates. These effects are captured within the presented function. The fault permeability is strongly dependent on the thickness of the damage zone, as well as the inter-connectedness and density of the fracture networks within the damage zone, and studies have demonstrated that these fault zone parameters are influenced by the pressure within the reservoir-caprock-fault system (Rutqvist 2012; Vilarrasa et al., 2017).

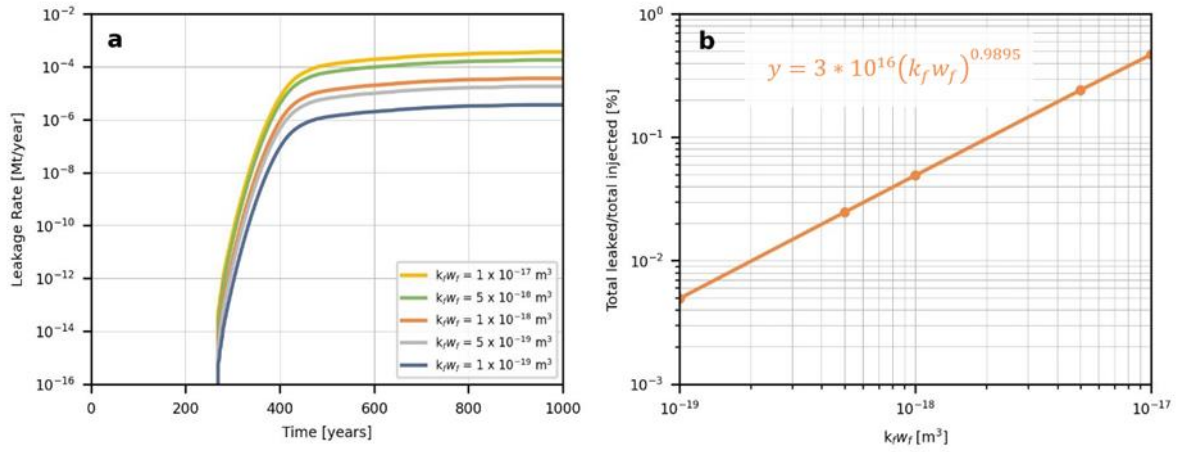

Figure 8 – Impact of fault properties on CO_2 leakage showing the relationship between fault permeability, damage zone thickness, and the magnitude of CO_2 leakage (a) and the decrease in total CO_2 leakage over time with decreasing value for the product of fault permeability and damage zone thickness $k_f w_f$ (b).

The capillary entry pressure of the fault is also an important factor to consider for leakage scenarios. High capillary entry pressure can prevent leakage, even where a fault is permeable (Monzocchi et al., 2010; Zheng & Espinoza, 2022). In the preceding simulation for the J area, the fault did not contain entry pressure that needed to be exceeded for CO_2 to leak. The impact of fault capillary entry pressure on leakage was tested by running a series of simulations with increasing fault capillary entry pressure, while keeping all other parameters the same as in Table 4. The resulting leakage rate profile is shown in Figure 9a. As the fault capillary entry pressure increases, the leakage rate decreases, and the onset of leakage is delayed. A fault capillary entry pressure of 1 bar is found to result in a fully sealing fault, with no CO_2 leakage observed for the given injection conditions. These results clearly demonstrate the importance of the fault capillary entry pressure and its significant impact on the leakage behavior. This parameter can be used to help determine the maximum safe storage capacity for a given fault condition. Figure 9b shows the maximum injection rate with zero leakage rate for a range of fault capillary entry pressures. For a fault with a capillary entry pressure of 0.5 bar, leakage is not observed for an injection rate of up to 0.5 MT per year, while for a capillary entry

pressure of 1.0 bar, leakage is not observed for an injection rate of up to 1.3 MT per year. This approach provides a valuable tool for screening the maximum safe injection rate and the maximum storage capacity at which the risk of CO_2 leakage along faults is small.

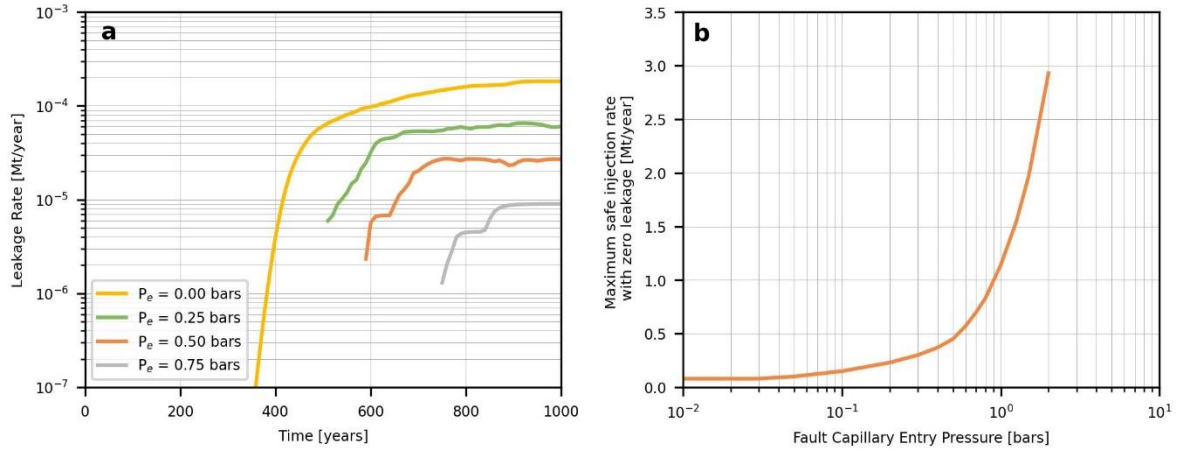

Figure 9 – Impact of fault capillary entry pressure on CO_2 leakage showing the leakage profile for different fault capillary entry pressures where higher entry pressures act as a barrier, delaying and reducing the CO_2 leakage and no leakage occurs for a scenario of 1 bar (a). Maximum injection rate with zero leakage for a range of fault capillary entry pressures where increasing the entry pressure allows for higher injection rates without CO_2 leakage (b).

4 Conclusions

This work presents a fast and computationally efficient tool for simulating fault leakage under uncertainty for realistic, field-scale CO_2 storage applications. Faults are inherently complex, typically characterized by a fault core and a surrounding fractured damage zone, both of which significantly influence fault leakage behavior at the field scale. Explicitly representing these fault complexities along with the multi-layered systems is a computationally intensive method for resolving fault leakage-related uncertainty, especially during the early stages of storage site screening when data availability is limited. The primary contribution of this work addresses this challenge by proposing an approach that integrates an upscaled fault leakage function, specifically tailored to the unique characteristics of the fault core, damage zone, and flow properties, into a VE reservoir modeling framework. This integration provides a valuable

tool for incorporating the geological understanding of faults into leakage assessment workflows. The computationally efficiency of our proposed approach enables the fast screening of a large number of geological scenarios inherent to multiple potential storage sites, identify those sites that are most promising to develop a secure storage project, and develop more targeted data acquisition and reservoir characterization studies for these sites. Such fast screening of potential storage sites is key to enable the scale-up of CO_2 and reach the gigaton storage needed to reduce global CO_2 emissions.

By applying this modeling framework to various CO_2 injection scenarios, we were able to gain insights into the key factors influencing fault-related leakage, such as fault permeability, capillary entry pressure, and the interaction between the fault and the surrounding reservoir. The results from these simulations offer valuable information for the design and risk assessment of CO_2 storage projects in geologically complex settings. While the assumption of constant fault properties simplifies the modeling approach, it may not capture the full heterogeneity and uncertainty associated with real-world fault systems. Future work could explore the impact of incorporating more detailed, stochastic representations of the fault hydraulic properties and geomechanical factors and constraints on the leakage estimates, further enhancing the reliability and applicability of the modeling framework.

Acknowledgements

The funding and data underpinning this work was provided by PETRONAS via the PETRONAS Centre of Excellence in Subsurface Engineering and Energy Transition (PACESET), based at Heriot-Watt University. Sebastian Geiger thanks Energi Simulation for supporting his Chair in Sustainable Geoenergy. Florian Doster acknowledge valuable discussions with Michael A. Celia, Jan M. Nordbotten and Mary Kang while formulating the research topic.

1 References

Abd Rahman, I. Z., Abang Hasbollah, D. Z., Mohd Yunus, N. Z., Kasiman, E. H., & Mazlan, A. N. (2022). Carbon dioxide storage potential in malaysian sandstone aquifer: An overview. *IOP Conference Series: Earth and Environmental Science*, *971*(1), 012022. https://doi.org/10.1088/1755-1315/971/1/012022

Andersen, O. (2017). *Simplified models for numerical simulation of geological CO2 storage* [Doctoral thesis, The University of Bergen]. https://bora.uib.no/bora-xmlui/handle/1956/15477

Andersen, O. A., Nilsen, H. M., & Gasda, S. E. (2016, August 29). *Modelling geomechanical impact of co2 injection and migration using precomputed response functions*. ECMOR XV - 15th European Conference on the Mathematics of Oil Recovery, Amsterdam, Netherlands. https://doi.org/10.3997/2214-4609.201601760

Andersen, O. A., Nilsen, H. M., & Gasda, S. E. (2017). Vertical equilibrium flow models with fully coupled geomechanics for co2 storage modeling, using precomputed mechanical response functions. *Energy Procedia*, *114*, 3113–3131. https://doi.org/10.1016/j.egypro.2017.03.1440

Andersen, O., Gasda, S. E., & Nilsen, H. M. (2015). Vertically averaged equations with variable density for co2 flow in porous media. *Transport in Porous Media*, *107*(1), 95–127. https://doi.org/10.1007/s11242-014-0427-z

Anderson, S. T. (2017). Risk, liability, and economic issues with long-term CO2 storage—A review. *Natural Resources Research*, *26*(1), 89–112. https://doi.org/10.1007/s11053-016-9303-6

Ashworth, P., Wade, S., Reiner, D., & Liang, X. (2015). Developments in public communications on CCS. *International Journal of Greenhouse Gas Control*, *40*, 449–458. https://doi.org/10.1016/j.ijggc.2015.06.002

Bachu, S. (2008). Legal and regulatory challenges in the implementation of CO2 geological storage: An Alberta and Canadian perspective☆. *International Journal of Greenhouse Gas Control*, *2*(2), 259–273. https://doi.org/10.1016/j.ijggc.2007.12.003

Ballas, G., Fossen, H., & Soliva, R. (2015). Factors controlling permeability of cataclastic deformation bands and faults in porous sandstone reservoirs. *Journal of Structural Geology*, *76*, 1–21. https://doi.org/10.1016/j.jsg.2015.03.013

Bandilla, K. W., Celia, M. A., & Leister, E. (2014). Impact of model complexity on co2 plume modeling at sleipner. *Energy Procedia*, *63*, 3405–3415. https://doi.org/10.1016/j.egypro.2014.11.369

Becker, B., Guo, B., Bandilla, K., Celia, M. A., Flemisch, B., & Helmig, R. (2017). A pseudo-vertical equilibrium model for slow gravity drainage dynamics. *Water Resources Research*, *53*(12), 10491–10507. https://doi.org/10.1002/2017WR021644

Becker, B., Guo, B., Bandilla, K., Celia, M. A., Flemisch, B., & Helmig, R. (2018). An adaptive multiphysics model coupling vertical equilibrium and full multidimensions for multiphase flow in porous media. *Water Resources Research*, *54*(7), 4347–4360. https://doi.org/10.1029/2017WR022303

Becker, B., Guo, B., Buntic, I., Flemisch, B., & Helmig, R. (2022). An adaptive hybrid vertical equilibrium/full-dimensional model for compositional multiphase flow. *Water Resources Research*, *58*(1), e2021WR030990. https://doi.org/10.1029/2021WR030990

Berge, R. L., Gasda, S. E., Keilegavlen, E., & Sandve, T. H. (2022). Impact of deformation bands on fault-related fluid flow in field-scale simulations. *International Journal of Greenhouse Gas Control*, *119*, 103729. https://doi.org/10.1016/j.ijggc.2022.103729

Bielicki, J. M., Pollak, M. F., Fitts, J. P., Peters, C. A., & Wilson, E. J. (2014). Causes and financial consequences of geologic CO2 storage reservoir leakage and interference with other subsurface resources. *International Journal of Greenhouse Gas Control*, 20, 272–284. https://doi.org/10.1016/j.ijggc.2013.10.024

Bjørnarå, T. I., Nordbotten, J. M., & Park, J. (2016). Vertically integrated models for coupled two-phase flow and geomechanics in porous media. *Water Resources Research*, *52*(2), 1398–1417. https://doi.org/10.1002/2015WR017290

Caine, J. S., Evans, J. P., & Forster, C. B. (1996). Fault zone architecture and permeability structure. *Geology*, *24*(11), 1025. https://doi.org/10.1130/0091-7613(1996)024<1025:FZAAPS>2.3.CO;2

Celia, M. A., Bachu, S., Nordbotten, J. M., & Bandilla, K. W. (2015). Status of CO_2 storage in deep saline aquifers with emphasis on modelling approaches and practical simulations. *Water Resources Research*, *51*(9), 6846–6892. https://doi.org/10.1002/2015WR017609

Childs, C., Manzocchi, T., Walsh, J. J., Bonson, C. G., Nicol, A., & Schöpfer, M. P. J. (2009). A geometric model of fault zone and fault rock thickness variations. *Journal of Structural Geology*, *31*(2), 117–127. https://doi.org/10.1016/j.jsg.2008.08.009

Climate Change Committee (2021). Independent assessment: The uk's net zero strategy. (n.d.). Climate Change Committee. Retrieved March 12, 2024, from https://www.theccc.org.uk/publication/independent-assessment-the-uks-net-zero-strategy/

de Jonge-Anderson, I., Ramachandran, H., Nicholson, U., Geiger, S., Widyanita, A., & Doster, F. (2024). Determining CO2 storage efficiency within a saline aquifer using reduced complexity models. *Advances in Geo-Energy Research*, *13*(1), 22–31. https://doi.org/10.46690/ager.2024.07.04

de Jonge-Anderson, I., Widyanita, A., Busch, A., Doster, F., & Nicholson, U. (2024). New insights into the structural and stratigraphic evolution of the Malay Basin using 3D seismic data: Implications for regional carbon capture and storage potential. *Basin Research*, 36(4), e12885. https://doi.org/10.1111/bre.12885

Department of Geology, Universiti Malaya, 50603 Kuala Lumpur, Malaysia, & Madon, M. (2021). Five decades of petroleum exploration and discovery in the malay basin (1968-2018) and remaining potential. *Bulletin Of The Geological Society Of Malaysia*, *72*, 63–88. https://doi.org/10.7186/bgsm72202106

Dewhurst, D. N., Delle Piane, C., Esteban, L., Sarout, J., Josh, M., Pervukhina, M., & Clennell, M. B. (2018). Microstructural, geomechanical, and petrophysical characterization of shale caprocks. In S. Vialle, J. Ajo-Franklin, & J. W. Carey (Eds.), *Geophysical Monograph Series* (1st ed., pp. 1–30). Wiley. https://doi.org/10.1002/9781119118657.ch1

Dixon, T., McCoy, S. T., & Havercroft, I. (2015). Legal and regulatory developments on ccs. *International Journal of Greenhouse Gas Control*, *40*, 431–448. https://doi.org/10.1016/j.ijggc.2015.05.024

Doster, F., Nordbotten, J. M., & Celia, M. A. (2012). Hysteretic upscaled constitutive relationships for vertically integrated porous media flow. *Computing and Visualization in Science*, *15*(4), 147–161. https://doi.org/10.1007/s00791-013-0206-3

Doster, F., Nordbotten, J. M., & Celia, M. A. (2013). Impact of capillary hysteresis and trapping on vertically integrated models for CO2 storage. *Advances in Water Resources*, *62*, 465–474. https://doi.org/10.1016/j.advwatres.2013.09.005

Du Plessis, E., Nordbotten, J. M., Gasda, S. E., & Dahle, H. K. (2013). Influence of capillary pressure and trapping hysteresis on large-scale CO₂

migration. *Journal of Coupled Systems and Multiscale Dynamics*, *1*(4), 442–458. https://doi.org/10.1166/jcsmd.2013.1030

Espinoza, D. N., & Santamarina, J. C. (2017). CO2 breakthrough—Caprock sealing efficiency and integrity for carbon geological storage. International Journal of Greenhouse Gas Control, 66, 218–229. https://doi.org/10.1016/j.ijggc.2017.09.019

Faulkner, D. R., Jackson, C. A. L., Lunn, R. J., Schlische, R. W., Shipton, Z. K., Wibberley, C. A. J., & Withjack, M. O. (2010). A review of recent developments concerning the structure, mechanics and fluid flow properties of fault zones. *Journal of Structural Geology*, *32*(11), 1557–1575. https://doi.org/10.1016/j.jsg.2010.06.009

Gasda, S. E., Nordbotten, J. M., & Celia, M. A. (2011). Vertically averaged approaches for CO $_2$ migration with solubility trapping. *Water Resources Research*, *47*(5), 2010WR009075. https://doi.org/10.1029/2010WR009075

Gasda, S. E., Stephansen, A. F., Aavatsmark, I., & Dahle, H. K. (2013). Upscaled modeling of co2 injection and migration with coupled thermal processes. *Energy Procedia*, *40*, 384–391. https://doi.org/10.1016/j.egypro.2013.08.044

Gasda, S., Keilegavlen, E., Sandve, T. H., Berge, R., Pettersson, P., & Krumscheid, S. (2022). Practical field-scale simulation approaches for quantification of fault-related leakage under uncertainty. *SSRN Electronic Journal*. https://doi.org/10.2139/ssrn.4277020

Gillespie, P. A., Howard, C. B., Walsh, J. J., & Watterson, J. (1993). Measurement and characterisation of spatial distributions of fractures. *Tectonophysics*, *226*(1–4), 113–141. https://doi.org/10.1016/0040-1951(93)90114-Y

Hasbollah, D. Z. A., Junin, R., Taib, A. M., & Mazlan, A. N. (2020). Basin evaluation of co2 geological storage potential in malay basin, malaysia. In P. Duc Long & N. T. Dung (Eds.), *Geotechnics for Sustainable Infrastructure Development* (Vol. 62, pp. 1405–1410). Springer Singapore. https://doi.org/10.1007/978-981-15-2184-3_184

Hepple, R. P., & Benson, S. M. (2005). Geologic storage of carbon dioxide as a climate change mitigation strategy: Performance requirements and the implications of surface seepage. *Environmental Geology*, *47*(4), 576–585. https://doi.org/10.1007/s00254-004-1181-2

Herzog, H. J. (2011). Scaling up carbon dioxide capture and storage: From megatons to gigatons. *Energy Economics*, *33*(4), 597–604. https://doi.org/10.1016/j.eneco.2010.11.004

Huppert, H. E., & Woods, A. W. (1995). Gravity-driven flows in porous layers. *Journal of Fluid Mechanics*, *292*, 55–69. https://doi.org/10.1017/S0022112095001431

Jha, B., & Juanes, R. (2014). Coupled modeling of multiphase flow and fault poromechanics during geologic co2 storage. *Energy Procedia*, *63*, 3313–3329. https://doi.org/10.1016/j.egypro.2014.11.360

Jones, D. G., Beaubien, S. E., Blackford, J. C., Foekema, E. M., Lions, J., De Vittor, C., West, J. M., Widdicombe, S., Hauton, C., & Queirós, A. M. (2015). Developments since 2005 in understanding potential environmental impacts of CO2 leakage from geological storage. *International Journal of Greenhouse Gas Control*, *40*, 350–377. https://doi.org/10.1016/j.ijggc.2015.05.032

Kang, M., Nordbotten, J. M., Doster, F., & Celia, M. A. (2014). Analytical solutions for two-phase subsurface flow to a leaky fault considering vertical flow effects and fault properties. *Water Resources Research*, *50*(4), 3536–3552. https://doi.org/10.1002/2013WR014628

Knipe, R. J., Jones, G., & Fisher, Q. J. (1998). Faulting, fault sealing and fluid flow in hydrocarbon reservoirs: An introduction. *Geological Society, London, Special Publications*, *147*(1). https://doi.org/10.1144/GSL.SP.1998.147.01.01

Krevor, S., De Coninck, H., Gasda, S. E., Ghaleigh, N. S., De Gooyert, V., Hajibeygi, H., Juanes, R., Neufeld, J., Roberts, J. J., & Swennenhuis, F. (2023). Subsurface carbon dioxide and hydrogen storage for a sustainable energy future. *Nature Reviews Earth & Environment*, *4*(2), 102–118. https://doi.org/10.1038/s43017-022-00376-8

Kumar, A., Ozah, R., Noh, M., Pope, G. A., Bryant, S., Sepehrnoori, K., & Lake, L. W. (2005). Reservoir simulation of co2 storage in deep saline aquifers. *SPE Journal*, *10*(03), 336–348. https://doi.org/10.2118/89343-PA

Lie, K.-A. (2019). *An introduction to reservoir simulation using matlab/gnu octave: User guide for the matlab reservoir simulation toolbox(Mrst)* (1st ed.). Cambridge University Press. https://doi.org/10.1017/9781108591416

Malaysian Continental Shelf Project, National Security Council, Malaysia, Madon, M., Jong, J., & JX Nippon Oil and Gas Exploration (Malaysia) Limited, Malaysia. (2021). Geothermal gradient and heat flow maps of offshore malaysia: Some updates and observations. *Bulletin of the Geological Society of Malaysia*, *71*, 159–183. https://doi.org/10.7186/bgsm71202114

Møll Nilsen, H., Herrera, P. A., Ashraf, M., Ligaarden, I., Iding, M., Hermanrud, C., Lie, K.-A., Nordbotten, J. M., Dahle, H. K., & Keilegavlen, E. (2011). Field-case simulation of CO2 -plume migration using vertical-equilibrium models. *Energy Procedia*, *4*, 3801–3808. https://doi.org/10.1016/j.egypro.2011.02.315

Møll Nilsen, H., Lie, K.-A., & Andersen, O. (2015). Analysis of CO2 trapping capacities and long-term migration for geological formations in the Norwegian North Sea using MRST-co2lab. *Computers & Geosciences*, *79*, 15–26. https://doi.org/10.1016/j.cageo.2015.03.001

Manzocchi, T., Childs, C., & Walsh, J. J. (2010). Faults and fault properties in hydrocarbon flow models. *Geofluids*, *10*(1–2), 94–113. https://doi.org/10.1111/j.1468-8123.2010.00283.x

Morris, J. P., Hao, Y., Foxall, W., & McNab, W. (2011). A study of injection-induced mechanical deformation at the In Salah CO2 storage project. *International Journal of Greenhouse Gas Control*, *5*(2), 270–280. https://doi.org/10.1016/j.ijggc.2010.10.004

Møyner, O., & Nilsen, H. M. (2019). Multiresolution coupled vertical equilibrium model for fast flexible simulation of CO2 storage. *Computational Geosciences*, *23*(1), 1–20. https://doi.org/10.1007/s10596-018-9775-z

Neufeld, J. A., Vella, D., & Huppert, H. E. (2009). The effect of a fissure on storage in a porous medium. *Journal of Fluid Mechanics*, *639*, 239–259. https://doi.org/10.1017/S0022112009991030

Nilsen, H. M., Lie, K.-A., & Andersen, O. (2016). Fully-implicit simulation of vertical-equilibrium models with hysteresis and capillary fringe. *Computational Geosciences*, *20*(1), 49–67. https://doi.org/10.1007/s10596-015-9547-y

Nilsen, H. M., Lie, K.-A., & Andersen, O. (2016). Robust simulation of sharp-interface models for fast estimation of CO2 trapping capacity in large-scale aquifer systems. *Computational Geosciences*, *20*(1), 93–113. https://doi.org/10.1007/s10596-015-9549-9

Nordbotten, J. M., & Celia, M. A. (2011). *Geological storage of co2: Modeling approaches for large-scale simulation* (1st ed.). Wiley. https://doi.org/10.1002/9781118137086

Nordbotten, J. M., & Dahle, H. K. (2011). Impact of the capillary fringe in vertically integrated models for CO $_2$ storage. *Water Resources Research*, *47*(2), 2009WR008958. https://doi.org/10.1029/2009WR008958

Oladyshkin, S., Class, H., Helmig, R., & Nowak, W. (2011). A concept for data-driven uncertainty quantification and its application to carbon dioxide storage in geological

formations. *Advances in Water Resources*, *34*(11), 1508–1518. https://doi.org/10.1016/j.advwatres.2011.08.005

Pawar, R. J., Bromhal, G. S., Carey, J. W., Foxall, W., Korre, A., Ringrose, P. S., Tucker, O., Watson, M. N., & White, J. A. (2015). Recent advances in risk assessment and risk management of geologic CO2 storage. *International Journal of Greenhouse Gas Control*, *40*, 292–311. https://doi.org/10.1016/j.ijggc.2015.06.014

Pawar, R. J., Bromhal, G. S., Chu, S., Dilmore, R. M., Oldenburg, C. M., Stauffer, P. H., Zhang, Y., & Guthrie, G. D. (2016). The National Risk Assessment Partnership's integrated assessment model for carbon storage: A tool to support decision making amidst uncertainty. *International Journal of Greenhouse Gas Control*, *52*, 175–189. https://doi.org/10.1016/j.ijggc.2016.06.015

Phillips, T., Kampman, N., Bisdom, K., Forbes Inskip, N. D., Den Hartog, S. A. M., Cnudde, V., & Busch, A. (2020). Controls on the intrinsic flow properties of mudrock fractures: A review of their importance in subsurface storage. *Earth-Science Reviews*, *211*, 103390. https://doi.org/10.1016/j.earscirev.2020.103390

Pruess, K. (2011). Integrated modeling of CO $_2$ storage and leakage scenarios including transitions between super- and subcritical conditions, and phase change between liquid and gaseous CO $_2$. *Greenhouse Gases: Science and Technology*, *1*(3), 237–247. https://doi.org/10.1002/ghg.24

Ramachandran, H., Pope, G. A., & Srinivasan, S. (2017). Numerical study on the effect of thermodynamic phase changes on co2 leakage. *Energy Procedia*, *114*, 3528–3536. https://doi.org/10.1016/j.egypro.2017.03.1482

Ringrose, P., & Bentley, M. (2021). *Reservoir model design: A practitioner's guide*. Springer International Publishing. https://doi.org/10.1007/978-3-030-70163-5

Ringrose, P. S., Mathieson, A. S., Wright, I. W., Selama, F., Hansen, O., Bissell, R., Saoula, N., & Midgley, J. (2013). The in salah co2 storage project: Lessons learned and knowledge transfer. *Energy Procedia*, *37*, 6226–6236. https://doi.org/10.1016/j.egypro.2013.06.551

Rizzo, R. E., Inskip, N. F., Fazeli, H., Betlem, P., Bisdom, K., Kampman, N., Snippe, J., Senger, K., Doster, F., & Busch, A. (2024). Modelling geological CO2 leakage: Integrating fracture permeability and fault zone outcrop analysis. *International Journal of Greenhouse Gas Control*, *133*, 104105. https://doi.org/10.1016/j.ijggc.2024.104105

Romanak, K., & Dixon, T. (2022). CO2 storage guidelines and the science of monitoring: Achieving project success under the California Low Carbon Fuel Standard CCS Protocol and other global regulations. *International Journal of Greenhouse Gas Control*, *113*, 103523. https://doi.org/10.1016/j.ijggc.2021.103523

Rutqvist, J. (2012). The geomechanics of co2 storage in deep sedimentary formations. *Geotechnical and Geological Engineering*, *30*(3), 525–551. https://doi.org/10.1007/s10706-011-9491-0

Saló-Salgado, L., Davis, S., & Juanes, R. (2023). Fault permeability from stochastic modeling of clay smears. *Geology*, *51*(1), 91–95. https://doi.org/10.1130/G50739.1

Seebeck, H., Nicol, A., Walsh, J. J., Childs, C., Beetham, R. D., & Pettinga, J. (2014). Fluid flow in fault zones from an active rift. *Journal of Structural Geology*, *62*, 52–64. https://doi.org/10.1016/j.jsg.2014.01.008

Sibson, R. H. (1977). Fault rocks and fault mechanisms. *Journal of the Geological Society*, *133*(3), 191–213. https://doi.org/10.1144/gsjgs.133.3.0191

Silva, J. A., Saló-Salgado, L., Patterson, J., Dasari, G. R., & Juanes, R. (2023). Assessing the viability of CO 2 storage in offshore formations of the Gulf of Mexico at a scale

relevant for climate-change mitigation. *International Journal of Greenhouse Gas Control*, *126*, 103884. https://doi.org/10.1016/j.ijggc.2023.103884

Snippe, J., Kampman, N., Bisdom, K., Tambach, T., March, R., Maier, C., Phillips, T., Inskip, N. F., Doster, F., & Busch, A. (2022). Modelling of long-term along-fault flow of CO2 from a natural reservoir. *International Journal of Greenhouse Gas Control*, *118*, 103666. https://doi.org/10.1016/j.ijggc.2022.103666

Snippe, J., Kampman, N., Bisdom, K., Tambach, T., March, R., Maier, C., Phillips, T., Forbes Inskip, N., Doster, F., & Busch, A. (2021). Modelling of long-term along-fault flow of co2 from a natural reservoir. *SSRN Electronic Journal*. https://doi.org/10.2139/ssrn.3816437

Tewari, R. D., Tan, C. P., & Sedaralit, M. F. (2023). A toolkit approach for carbon capture and storage in offshore depleted gas field. *American Journal of Environmental Sciences*, *19*(1), 8–42. https://doi.org/10.3844/ajessp.2023.8.42

Tueckmantel, C., Fisher, Q. J., Manzocchi, T., Skachkov, S., & Grattoni, C. A. (2012). Two-phase fluid flow properties of cataclastic fault rocks: Implications for CO2 storage in saline aquifers. *Geology*, *40*(1), 39–42. https://doi.org/10.1130/G32508.1

Vilarrasa, V., Makhnenko, R. Y., & Laloui, L. (2017). Potential for fault reactivation due to co2 injection in a semi-closed saline aquifer. *Energy Procedia*, *114*, 3282–3290. https://doi.org/10.1016/j.egypro.2017.03.1460

Walsh, J. J., Watterson, J., Heath, A. E., & Childs, C. (1998). Representation and scaling of faults in fluid flow models. *Petroleum Geoscience*, *4*(3), 241–251. https://doi.org/10.1144/petgeo.4.3.241

White, J. A., Chiaramonte, L., Ezzedine, S., Foxall, W., Hao, Y., Ramirez, A., & McNab, W. (2014). Geomechanical behavior of the reservoir and caprock system at the In Salah CO_2 storage project. *Proceedings of the National Academy of Sciences*, *111*(24), 8747–8752. https://doi.org/10.1073/pnas.1316465111

Yortsos, Y. C. (1995). A theoretical analysis of vertical flow equilibrium. *Transport in Porous Media*, *18*(2), 107–129. https://doi.org/10.1007/BF01064674

Zheng, X., & Espinoza, D. N. (2022). Stochastic quantification of CO2 fault sealing capacity in sand-shale sequences. *Marine and Petroleum Geology*, *146*, 105961. https://doi.org/10.1016/j.marpetgeo.2022.105961